

## Supporting Information

### Nanometer-Scale Lateral p–n Junctions in Graphene/ $\alpha$ -RuCl<sub>3</sub> Heterostructures

Daniel J. Rizzo<sup>1,†</sup>, Sara Shabani<sup>1,†</sup>, Bjarke S. Jessen<sup>1,2,†</sup>, Jin Zhang<sup>3,†</sup>, Alexander S. McLeod<sup>1,#</sup>,  
Carmen Rubio-Verdú<sup>1</sup>, Francesco L. Ruta<sup>1,4</sup>, Matthew Cothrine<sup>5</sup>, Jiaqiang Yan<sup>5,6</sup>, David G.  
Mandrus<sup>5,6</sup>, Stephen E. Nagler<sup>7</sup>, Angel Rubio<sup>3,8,9,\*</sup>, James C. Hone<sup>2</sup>, Cory R. Dean<sup>1</sup>, Abhay N.  
Pasupathy<sup>1,10\*</sup>, D. N. Basov<sup>1,\*</sup>

<sup>1</sup>Department of Physics, Columbia University, New York, NY, 10027, USA

<sup>2</sup>Department of Mechanical Engineering, Columbia University, New York, NY, 10027, USA

<sup>3</sup>Theory Department, Max Planck Institute for Structure and Dynamics of Matter and Center for Free-Electron Laser Science, 22761 Hamburg, Germany

<sup>4</sup>Department of Applied Physics and Applied Mathematics, Columbia University, New York, NY, 10027, USA

<sup>5</sup>Department of Materials Science and Engineering, University of Tennessee, Knoxville, Tennessee 37996, USA

<sup>6</sup>Materials Science and Technology Division, Oak Ridge National Laboratory, Oak Ridge, Tennessee 37831, USA

<sup>7</sup>Neutron Scattering Division, Oak Ridge National Laboratory, Oak Ridge, Tennessee 37831, United States

<sup>8</sup>Center for Computational Quantum Physics, Flatiron Institute, New York, New York 10010, USA

<sup>9</sup>Nano-Bio Spectroscopy Group, Universidad del País Vasco UPV/EHU, San Sebastián 20018, Spain

<sup>10</sup>Condensed Matter Physics and Materials Science Department, Brookhaven National Laboratory, Upton, NY 11973, USA

<sup>†</sup>Contributed equally

<sup>#</sup>Present Address: School of Physics and Astronomy, University of Minnesota, Minneapolis, MN 55455

\*Correspondence to: db3056@columbia.edu, apn2108@columbia.edu, and angel.rubio@mpsd.mpg.de

**Table of Contents:**

<b>Figure S1. Graphene/<math>\alpha</math>-RuCl<sub>3</sub> device fabrication</b>	S3
<b>Figure S2. STM and AFM topographic data</b>	S4
<b>Figure S3. STM and STS of multiple nanobubbles</b>	S5
<b>Figure S4. s-SNOM on multiple nanobubbles with <math>\omega</math>- and angle-dependent near-field linecuts</b>	S6
Supplementary Methods	S7
Supplementary Discussion	S9
<b>References</b>	S15

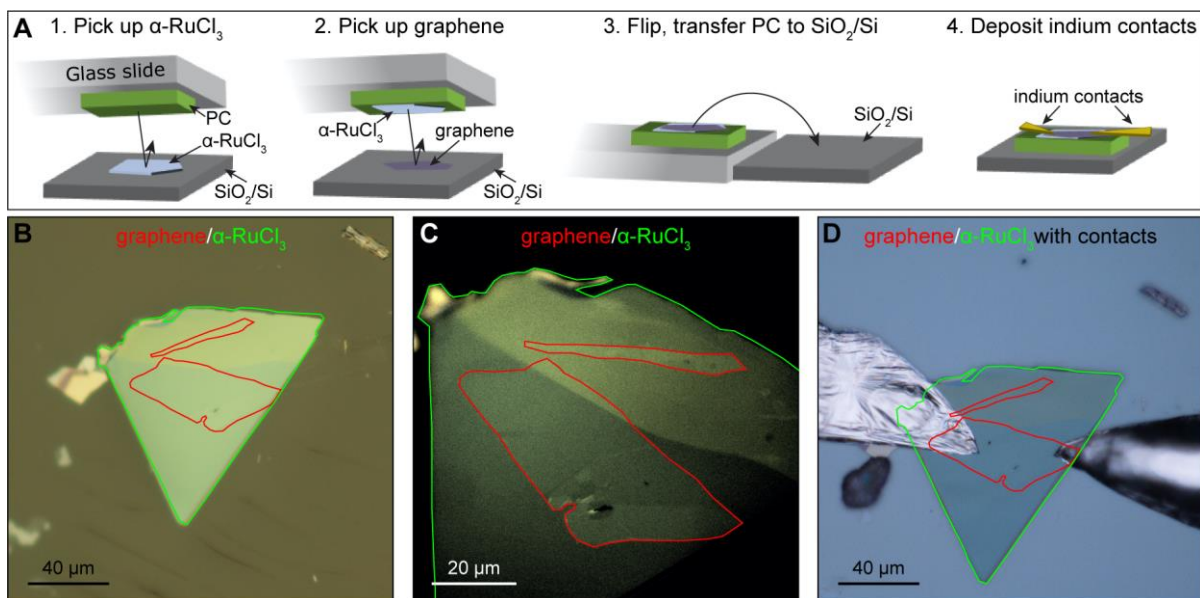


**Figure S1. Graphene/ $\alpha$ -RuCl<sub>3</sub> device fabrication.** (A) Diagram of four steps for graphene/ $\alpha$ -RuCl<sub>3</sub> device assembly. In the first step, a PC-coated glass slide is used to pick up exfoliated  $\alpha$ -RuCl<sub>3</sub> on an SiO<sub>2</sub>/Si substrate. In the second step, the  $\alpha$ -RuCl<sub>3</sub>/PC transfer slide is used to pick up exfoliated graphene. In the third step, the transfer slide is flipped over and the PC is delaminated from the glass slide and placed on a SiO<sub>2</sub>/Si chip. In the final step, indium contacts are deposited on the device using a micro soldering approach.<sup>1</sup> (B) Optical image of graphene/ $\alpha$ -RuCl<sub>3</sub> device with the graphene outlined in red and the  $\alpha$ -RuCl<sub>3</sub> outlined in green. (C) High contrast magnified image of the stack shown in (B). (D) Optical image of the graphene/ $\alpha$ -RuCl<sub>3</sub> device after the deposition of indium contacts.

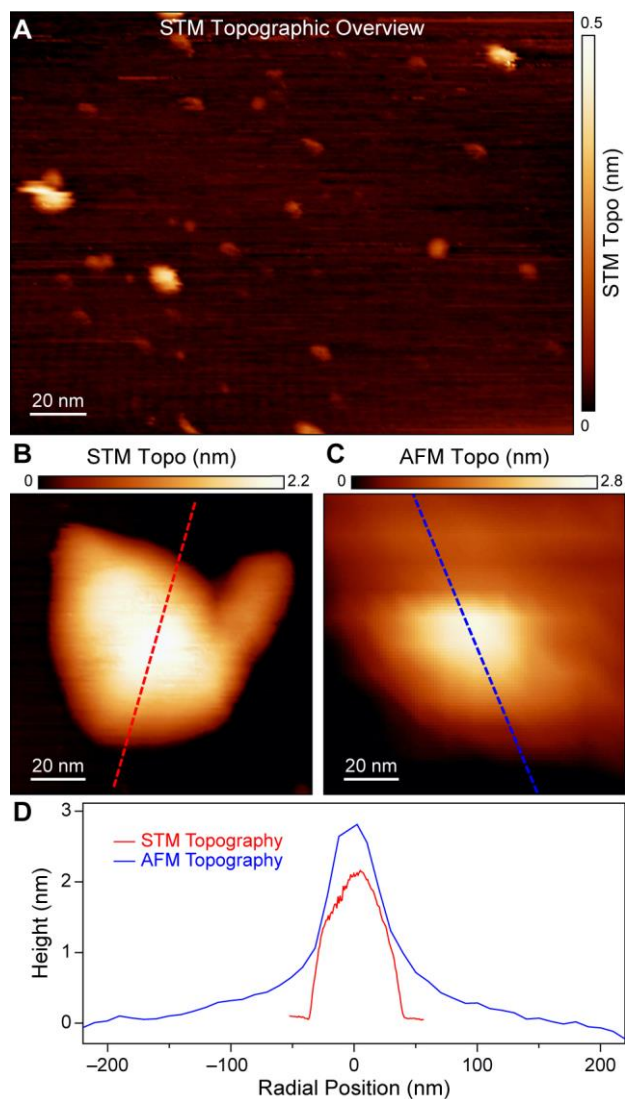


**Figure S2. STM and AFM topographic data.** (A) STM topographic overview of graphene/ $\alpha$ -RuCl<sub>3</sub> ( $V_s = 0.7$  V,  $I_t = 50$  pA) showing that both flat regions and nanobubbles are present. (B) High magnification STM topographic image of a typical graphene nanobubble ( $V_s = 0.7$  V,  $I_t = 50$  pA). (C) High magnification AFM topographic image of a typical graphene nanobubble. (D) Topographic line profiles based on the images in (B) and (C) showing that typical nanobubbles measured in STM (red curve) have a similar topography to those viewed with AFM and s-SNOM (blue curve).

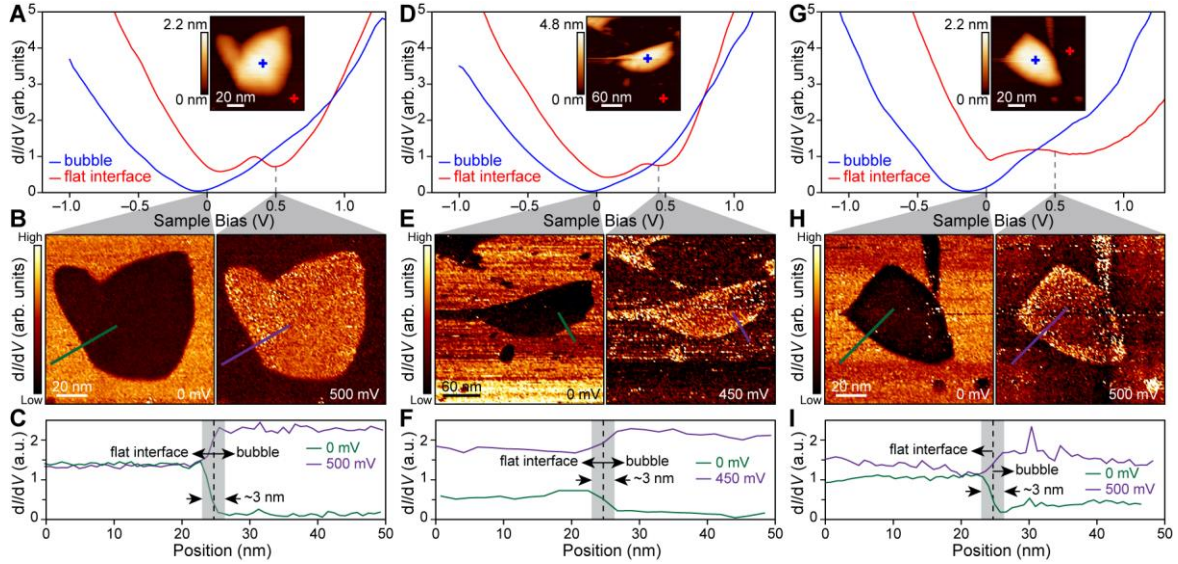


**Figure S3. STM and STS of multiple nanobubbles.** (A) Inset: STM topographic image of a second graphene nanobubble ( $V_s = 0.7$  V,  $I_t = 50$  pA). Representative  $dI/dV$  point spectroscopy collected over nanobubbles (blue curve) and flat graphene/ $\alpha$ -RuCl<sub>3</sub> interfaces (red curve) as indicated by the crosshairs in the inset. (B)  $dI/dV$  maps of a graphene nanobubble conducted at the indicated biases corresponding to the Dirac point energies on the nanobubble (left panel) and the flat interface (right panel) ( $V_{AC} = 25$  mV,  $I_t = 50$  pA). A suppressed LDOS is observed at those biases associated with the local Dirac point energy. (C) Linecuts of the  $dI/dV$  maps shown in (B) following the green and purple lines indicated on the 0 mV and 500 mV maps, respectively. In both instances, the change in the LDOS at the bubble boundary (indicated by the black dashed line) takes place over a lateral length of approximately 3 nm. (D), (E), and (F) same as (A), (B), and (C), respectively, but for a third graphene nanobubble. (G), (H), and (I) same as (A), (B), and (C), respectively, but for a fourth graphene nanobubble.

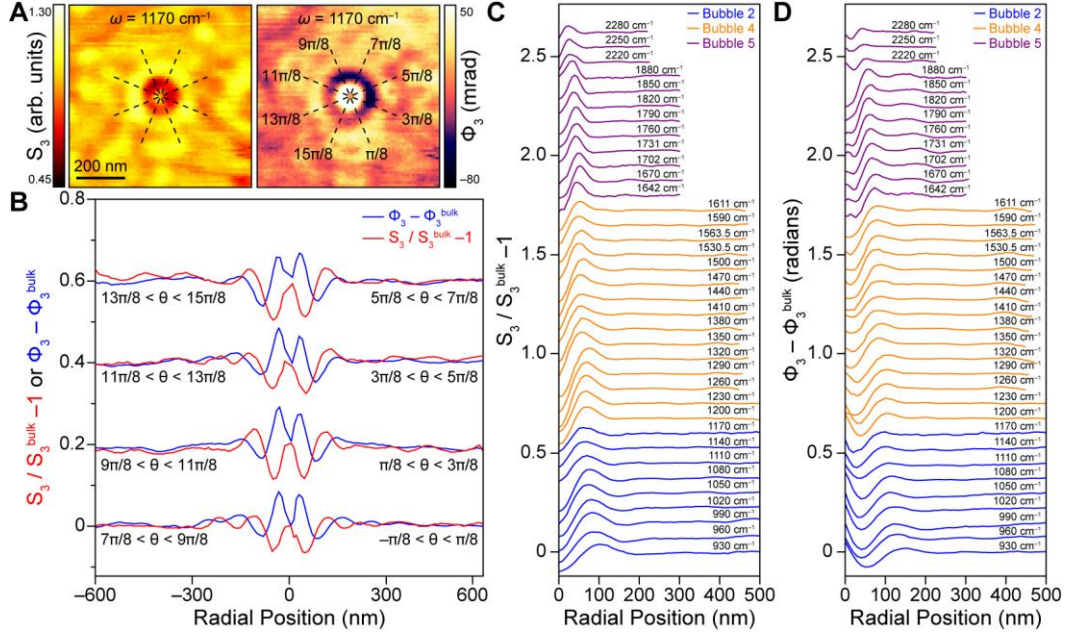


**Figure S4. s-SNOM on multiple nanobubbles with  $\omega$ - and angle-dependent near-field linecuts.** (A) s-SNOM  $S_3$  amplitude (left panel) and  $\Phi_3$  phase (right panel) collected over a graphene nanobubble ( $\omega = 1170 \text{ cm}^{-1}$ ). The black dashed lines separate the s-SNOM maps into eight angular slices used for the analysis in (B). (B) The radial dependence of the s-SNOM  $S_3$  amplitude (red curves) and  $\Phi_3$  phase (blue curves) integrated over the indicated angles designated in (A). The lack of a systematic angular dependence suggests that  $\lambda_p$  fringes do not contribute significantly to the plasmonic response of nanobubbles. (C) The radial dependence of the  $S_3$  amplitude is shown for frequencies spanning  $\omega = 930 \text{ cm}^{-1} - 2280 \text{ cm}^{-1}$  collected on bubble 2 (blue curves), bubble 4 (orange curves) and bubble 5 (purple curves) referenced in Figure 3 of the main manuscript. Since bubbles 1, 2, and 3 all overlap in frequency, only bubble 2 is shown for clarity. All line profiles are truncated at the boundary of the associated nanobubble. (D) Same as (C) but for the radial dependence of the  $\Phi_3$  phase.

## Supplementary Methods

### Material Growth:

$\alpha$ -RuCl<sub>3</sub> crystals were grown by the sublimation of RuCl<sub>3</sub> powder sealed in a quartz tube under vacuum. About 1 g of powder was loaded in a quartz tube of 19 mm in outer diameter, 1.5 mm thick, and 10 cm long. The growth was performed in a box furnace. After dwelling at 1060 °C for 6 h, the furnace was cooled to 800 °C at a rate of 4 °C/h. Magnetic and specific heat measurements confirmed that the as-grown pristine crystal orders antiferromagnetically around 7 K. For more information, see ref. <sup>2</sup>.

### Device Fabrication:

$\alpha$ -RuCl<sub>3</sub> is notoriously difficult to pick up using standard dry stacking techniques. To overcome this limitation, we modify the usual dry stacking procedure in the following ways: When exfoliating  $\alpha$ -RuCl<sub>3</sub> onto SiO<sub>2</sub>, we avoid any plasma treatment of the SiO<sub>2</sub> prior to exfoliation. This reduces the adhesion of the  $\alpha$ -RuCl<sub>3</sub> to the SiO<sub>2</sub> (albeit at the expense of the yield of large-area crystals, which were not needed in this experiment).

To pick up the  $\alpha$ -RuCl<sub>3</sub>, we employ PDMS stamps coated with poly(bisphenol A carbonate) (PC). The PC is heated above the glass-transition temperature ( $T_g \approx 150$  °C) to 170 °C, leaving the film in a low viscosity state. We then slowly cover the target  $\alpha$ -RuCl<sub>3</sub> flake and leave the PC in contact with the  $\alpha$ -RuCl<sub>3</sub> for at least 10 minutes to ensure high coverage. Next, we lower the temperature to below  $T_g$ , solidifying the PC film around the  $\alpha$ -RuCl<sub>3</sub> crystal and significantly increasing the chance of a successful pick-up. We note that the temperature should not be raised higher than the values provided here, as the  $\alpha$ -RuCl<sub>3</sub> will readily decompose in ambient at temperatures above 200 °C. After the  $\alpha$ -RuCl<sub>3</sub> is successfully picked up, we can use more standard parameters to subsequently pick up other 2D materials (*e.g.*, graphene). Using this approach,  $\alpha$ -RuCl<sub>3</sub> flakes and single-layer graphene were sequentially lifted from SiO<sub>2</sub>/Si substrates using a PC coated glass transfer slide. The PC together with the stack were flipped onto an Si/SiO<sub>2</sub> (285 nm Si) substrate held at 150 °C. Indium alloy contacts were placed on the graphene using a micro soldering technique<sup>1</sup> to provide electrical contacts for STM measurements. This technique preserves sample quality compared to lithography methods. See Figure S1 for diagrammatic procedure.

### Scanning Tunneling Microscopy and Spectroscopy:

All STM/STS measurements were carried out on a commercial RHK system under ultra-high vacuum conditions. An etched Tungsten tip was prepared and calibrated on a Au(111) single crystal. The topographic images were collected in constant current and bias mode using a feedback loop. The STS point spectra were obtained at constant height under open feedback loop conditions with a modulating bias of 25 mV using a lock-in amplifier.  $dI/dV$  maps were extracted from a grid of individual point spectra collected in the vicinity of nanobubbles. All measurements were performed at room temperature to permit direct tunneling into  $\alpha$ -RuCl<sub>3</sub> (which is otherwise too resistive at cryogenic temperatures to permit local tunneling measurements).

### Scanning Near-Field Optical Microscopy:

All s-SNOM measurements were conducted using a commercial Neaspec system under ambient conditions using commercial Arrow<sup>TM</sup> AFM probes with a nominal resonant frequency

of  $f = 75$  kHz. Three tunable continuous wave quantum cascade lasers produced by Daylight Solutions were used, collectively spanning wavelengths from 4 to 11  $\mu\text{m}$ . The detected signal was demodulated at the third harmonic of the tapping frequency in order to minimize background contributions to the scattered light. Simultaneous measurement of the scattering amplitude and phase was performed through use of a pseudoheterodyne interferometer.

#### Ab-initio Calculations of Graphene/ $\alpha$ -RuCl<sub>3</sub> Heterostructures:

The *ab initio* calculations were performed within the Vienna Ab initio Simulation Package (VASP)<sup>3</sup> using a projector-augmented wave (PAW) pseudopotential in conjunction with the Perdew–Burke–Ernzerhof (PBE)<sup>4</sup> functionals and a plane-wave basis set with an energy cutoff at 400 eV. For the heterostructures with graphene and monolayer  $\alpha$ -RuCl<sub>3</sub>, we used a hexagonal supercell containing 82 atoms (composed of a  $5 \times 5$  graphene supercell and  $\sqrt{3} \times \sqrt{3}$   $\alpha$ -RuCl<sub>3</sub> supercell). The resulting strain is  $\sim 2.5\%$  for the  $\alpha$ -RuCl<sub>3</sub> monolayer. The surface Brillouin zone was sampled by a  $3 \times 3 \times 1$  Monkhorst–Pack k-mesh. A vacuum region of 15 Å was applied to avoid artificial interaction between the periodic images along the z direction. Because of the absence of strong chemical bonding between layers, van der Waals density functional in the opt88 form<sup>5</sup> was employed for structural optimization. All structures were fully relaxed until the force on each atom was less than 0.01 eV Å<sup>-1</sup>. Spin-orbital couplings are included in the electronic calculations.

With small Bader charges of 7.01 e (out of 8 e) per orbital, the Ru-4d states cannot be considered fully localized, and therefore, the use of large values of  $U_{4d}$  is understood as an *ad hoc* fitting parameter without physical basis. Instead, each Chlorine 3p orbital charge is 7.34 e (out of 7 e), indicating the importance of employing correction on both Ru and Cl elements. The Hubbard U terms are computed by employing the generalized Kohn–Sham equations within density functional theory including mean-field interactions, as provided by the Octopus package<sup>6,7</sup> using the ACBN0<sup>8,9</sup> functional together with the local density approximation (LDA) functional describing the semilocal DFT part. We compute *ab initio* the Hubbard U and Hund's J for the 4d orbitals of Ruthenium and 3p orbital of Chlorine. We employ norm-conserving HGH pseudopotentials to get converged effective Hubbard U values (1.96 eV for Ru 4d orbitals and 5.31 eV for Cl 3p orbitals) with spin-orbital couplings.

## Supplementary Discussion

### Modeling near-field signal from plasmon reflection at a finite-sized bubble defect

As attested by our experimental results, we model the plasmonic response of a single nanobubble in the graphene/ $\alpha$ -RuCl<sub>3</sub> heterostructure by a local perturbation of the graphene sheet conductivity  $\sigma$  with respect to its asymptotic value  $\sigma(\infty)$  arising from charge transfer from the  $\alpha$ -RuCl<sub>3</sub> underlayer. We denote the relative inhomogeneity in conductivity due the nanobubble as  $\bar{\sigma}(\mathbf{r}) = \sigma(\mathbf{r})/\sigma(\infty)$ . To model the position-dependent near-field signal associated with reflections of plasmon polaritons from the defect, we considered the integro-differential equation for the scalar potential  $\phi_s$  generated in response to the incident potential  $\phi_{\text{probe}}$  of a near-field probe<sup>10</sup>:

$$\left[1 + \frac{1}{2\pi q_s} V * \nabla \cdot \bar{\sigma}(\mathbf{r}) \nabla\right] \phi(\mathbf{r}) = \phi_{\text{probe}}(\mathbf{r}), \quad \phi = \phi_{\text{probe}} + \phi_s. \quad (\text{S1})$$

Here  $q_s = i\omega/(2\pi\sigma(\infty))$  parameterizes the asymptotic conductivity away from the defect through its associated plasmon polariton momentum,  $V(r) = 1/(\kappa r)$  is the Coulomb kernel screened by permittivity  $\epsilon$  of the proximate  $\alpha$ -RuCl<sub>3</sub> underlayer with  $\kappa = (\epsilon + 1)/2$ , and the asterisk (\*) denotes the spatial convolution over the in-plane coordinate  $\mathbf{r} = (x, y)$ . As an example, we choose  $\bar{\sigma}(\mathbf{r}) \equiv 1 + \delta\Lambda(r/R_{\text{bubble}})$ , where  $\delta$  is the characteristic magnitude of the conductivity fluctuation at the nanobubble,  $R_{\text{bubble}}$  is its width, and  $\Lambda(r) = 1 - \theta(r - 1)$  is taken as a step function of unit radius and height. We solved Eq. (S1) through expansion in an orthonormal basis of plane waves  $\phi_j = A_j e^{i\mathbf{q}_j \cdot \mathbf{r}}$  periodic in a 2D square cell  $x, y \in [-L/2, L/2]$ , with  $A_j$  a normalization constant and  $L \gg R_{\text{bubble}}$ . If we assemble the Fourier momenta  $\mathbf{q}_j$  and the Fourier coefficients  $\tilde{\phi}_j = \langle \phi_j | \phi \rangle \equiv \int \phi_j^*(\mathbf{r}) \phi(\mathbf{r}) d^2r$  into column vectors  $\vec{q}$  and  $\vec{\phi}$ , respectively, then  $\langle \phi_i | V * | \phi_j \rangle = 2\pi/(\kappa q_i) \delta_{ij}$  with  $\delta_{ij}$  the Kronecker delta, and these vectors must obey the equation

$$\vec{\phi} = [q_s^* - (\delta\vec{Q} + \text{diag} |\vec{q}|)]^{-1} q_s^* \vec{\phi}_{\text{probe}}, \quad (\text{S2})$$

where  $q_s^* = \kappa q_s$  defines the screened polariton momentum, and  $\vec{Q}$  is the scattering matrix with the elements

$$Q_{ij} = (\hat{\mathbf{q}}_i \cdot \mathbf{q}_j) \left\langle \phi_i \left| \Lambda\left(\frac{r}{R_{\text{bubble}}}\right) \right| \phi_j \right\rangle. \quad (\text{S3})$$

We defined another matrix-valued function  $\vec{G}$  by  $\vec{\phi}_s = \vec{G} \vec{\phi}_{\text{probe}}$ . From Eq. (S2), we obtain

$$G_{ij} = \left\langle \phi_i \left| [q_s^* - (\delta\vec{Q} + \text{diag} |\vec{q}|)]^{-1} (\delta\vec{Q} + \text{diag} |\vec{q}|) \right| \phi_j \right\rangle. \quad (\text{S4})$$

For a translationally invariant system,  $\delta = 0$ , where the momentum is conserved, only the diagonal matrix elements are nonzero. They can be understood as ‘‘in-plane’’ reflection coefficients, and are related to the conventional Fresnel coefficients  $r_p(\omega, q)$  by  $-G_{jj} =$

$r_p(\omega, q = |\mathbf{q}_j|)$ . Therefore,  $\text{Im}(-G_{jj}) = f(\omega, \mathbf{q}_j)$  has maxima at the same plasmon polariton momenta  $|\mathbf{q}_j| = \text{Re } q_s^*$  as  $\text{Im } r_p$ . However, our interest concerns  $\delta \neq 0$ .

Previous work<sup>11</sup> has established a leading order approximation to the complex-valued near-field signal  $\rho$  scattered by a probe, given by the Fourier integral:

$$\rho \sim -\frac{1}{2\pi} \int d^2q |\mathbf{q}| \tilde{\phi}_{\text{probe}}(\mathbf{q}) \tilde{\phi}_s(\mathbf{q}) \quad (\text{S5})$$

where  $\tilde{\phi}_{\text{probe}}$  and  $\tilde{\phi}_s$  denote Fourier transforms of the respective potentials with respect to in-plane (vector) momenta  $\mathbf{q}$  evaluated at the surface plane of the sample. The notation  $\rho$  used here for the near-field signal affirms its connection to the so-called photonic density of states as motivated in ref. <sup>11</sup>. In our case where  $\mathbf{q}_j$  describe a uniformly spaced grid of momenta spanning the “first Brillouin zone” of the simulation domain, Eq. (S5) is readily evaluated by:

$$\rho \sim \frac{1}{2\pi} \vec{\phi}_{\text{probe}}^T \text{diag } |\vec{q}| \vec{G}(q_s^*, R_{\text{bubble}}) \vec{\phi}_{\text{probe}}. \quad (\text{S6})$$

Here we highlight that the dependence on screened plasmon wavevector and nanobubble size resides in  $\vec{G}(q_s^*, R_{\text{bubble}})$ , which encodes the associated inhomogeneous optical response.

We developed a Python-language computer code implementing the above equations taking advantage of public-domain libraries and we used it to carry out a series of numerical simulations. For simplicity, we approximated  $\phi_{\text{probe}}(\mathbf{r})$  by a potential of a point dipole placed a small distance  $z_{\text{probe}}$  away from graphene<sup>12</sup>. Given an in-plane probe position  $\mathbf{r}_{\text{probe}}$ , the relative strength  $\delta$  of the perturbation due to the nanobubble, and the nanobubble radius  $R_{\text{bubble}}$ , the code computes the complex-valued amplitude and phase of  $\rho$ . We take  $z_{\text{probe}} \approx a \approx 30$  nm to appropriately treat the incident field from the near-field probe with apex radius  $a$ . Informed by our STS results demonstrating near uniform suppression (on the scale of both  $a$  and the unperturbed polariton wavelength) of the graphene Fermi level to near the Dirac point across the entire nanobubble, we take  $\delta \approx -1$  to denote complete suppression of free carrier conductivity. Meanwhile, as a representative case, we select  $R_{\text{bubble}} = 30$  nm  $\approx a$ . Results presented in Figure 3B of the main text were obtained by computing  $\rho$  for numerous values of  $q_s^*$  and the probe position  $r \equiv |\mathbf{r}_{\text{probe}}|$ , and normalizing the result by its value at  $\rho(r \rightarrow \infty)$ , thus highlighting contrasts due solely to the nanobubble-scattered field. The result can be straightforwardly understood as uniquely a function of three dimensionless ratios,  $z_{\text{probe}}/R_{\text{bubble}}$ ,  $\lambda_p/R_{\text{bubble}}$ , and  $r/R_{\text{bubble}}$ , where  $\lambda_p \equiv 2\pi/q_s^*$  defines the wavelength of the plasmon polariton in the bulk of graphene. The select results shown in Figure 3B of the main text are broadly characteristic of the case where  $z_{\text{probe}} \sim R_{\text{bubble}}$ , and are therefore well representative of the infrared nano-imaging results for nanobubbles characterized in this work.

### Derivation of scattering amplitude for plasmonic point-scatterer

In this section we utilize notations common to the previous section, where possible. The polariton scattering problem Eq. (S1) admits an analytic solution for the total field  $\phi = \phi_{\text{probe}} + \phi_s$  in the case that the excitation field  $\phi_{\text{probe}}$  and the “defect” in graphene optical conductivity

$\Delta\bar{\sigma}(\mathbf{r}) = \bar{\sigma}(\mathbf{r}) - 1$  take the form of a point source and a point scatterer, respectively. Provided that the defect and source are “not too strong”, a perturbation theory can be applied. The condition for its self-consistency will be discussed in the context of the result. In this case, it is convenient to rewrite Eq. (S1) in an operator notation:

$$\begin{aligned} [1 - (\hat{L}_0 + \epsilon \cdot \hat{L}')] \phi &= \phi_{\text{probe}} \\ \text{where } \hat{L}_0 &\equiv -\frac{1}{2\pi q_s} V * \nabla^2 \quad \text{and} \quad \hat{L}' \equiv -\frac{1}{2\pi q_s} V * \nabla \cdot \frac{1}{\epsilon} \Lambda(\mathbf{r} - \mathbf{r}_0) \nabla. \end{aligned} \quad (\text{S7})$$

Here  $\Lambda(\mathbf{r}) \approx A_s \delta(\mathbf{r})$  denotes the profile selected to describe the defect centered at lateral coordinate  $\mathbf{r}_0$ , with  $A_s$  its integral weight, in units of area, and  $\delta(\mathbf{r})$  a Dirac delta function. Meanwhile, taking  $\epsilon \ll 1$  supplies a perturbation expansion provided that  $\hat{L}' \phi_{\text{probe}}$  remains “small”:

$$\begin{aligned} \phi &= [1 - (\hat{L}_0 + \epsilon \cdot \hat{L}')]^{-1} \phi_{\text{probe}} \\ &\approx [\hat{G}_0 + \epsilon \hat{G}_0 \hat{L}' \hat{G}_0 + O(\epsilon^2)] \phi_{\text{probe}}, \\ &\quad \text{with } \hat{G}_0 \equiv (1 - \hat{L}_0)^{-1}. \end{aligned} \quad (\text{S8})$$

Here  $\hat{G}_0$  defines a “bare” propagator for plasmon polaritons. This propagator can be obtained through a Fourier representation of Eq. (S7) with respect to the in-plane wavevector  $\mathbf{q}$ , whereby:

$$\phi(\mathbf{r}) = \int \frac{d^2 q}{2\pi} e^{i\mathbf{q} \cdot \mathbf{r}} \phi(\mathbf{q}), \quad \phi(\mathbf{r}) = \int \frac{d^2 q}{2\pi} e^{i\mathbf{q} \cdot \mathbf{r}} \phi(\mathbf{q}), \quad \text{and} \quad \hat{L}_0 = |\mathbf{q}|/q_s^*. \quad (\text{S9})$$

Here we use the unitary Fourier transform. In the Fourier domain, the propagator is naively then expressed by  $G_0(q) = q_s^*/(q_s^* - q)$ . However, note that this form of the propagator  $\hat{G}_0 \phi_{\text{probe}}$  can only generate the inhomogeneous part of solutions  $\phi$ , to which any arbitrary homogeneous part  $\phi_h$  for which  $(1 - \hat{L}_0)\phi_h = 0$  can also be added (*e.g.*,  $\phi = \hat{G}_0 \phi_{\text{probe}} + \phi_h$ ) however necessary to satisfy the prescribed boundary conditions. For the case of an open system of graphene on  $\alpha$ -RuCl<sub>3</sub> illuminated by a localized probe, we will demand an outgoing radiation condition for  $\phi$ . In other words,  $\phi$  must vanish at infinite distance, and (polariton) waves must propagate outwards, with complex phase decreasing uniformly with distance from the source. To this end, we can augment the propagator as follows to enforce this condition. We first consider a point source placed at the origin,  $\phi_{\text{probe}}(\mathbf{r}) = A_p \delta(\mathbf{r})$ , where  $A_p$  denotes the integral weight of the excitation (in units of area), for which  $\phi_{\text{probe}}(q) = A_p/2\pi$ . The inhomogeneous part of the solution is given by:

$$\begin{aligned} [\hat{G}_0 \phi_{\text{probe}}](\mathbf{r}) &= \frac{A_p}{2\pi} \int \frac{d^2 q}{2\pi} e^{i\mathbf{q} \cdot \mathbf{r}} G(q) \\ &= \frac{A_p}{(2\pi)^2} \int_0^\infty dq q \left( \frac{q_s^*}{q_s^* - q} \right) \int_0^{2\pi} d\theta e^{iqr \cos \theta} \end{aligned}$$

$$\begin{aligned}
&= -\frac{A_p q_s^*}{2\pi} \int_0^\infty dq \frac{q}{q - q_s^*} J_0(qr) \\
&= -\frac{A_p q_s^{*2}}{2\pi} \left[ \frac{1}{q_s^* r} - \frac{\pi}{2} (Y_0(q_s^* r) + \mathbf{H}_0(q_s^* r)) \right]
\end{aligned} \tag{S10}$$

Here we have applied identity (2.12.3.11) of ref. <sup>13</sup> to the case of the Bessel function of order  $\nu = 0$ , where  $J_0(\dots)$ ,  $Y_0(\dots)$  and  $\mathbf{H}_0(\dots)$  denote Bessel functions of the first and second kinds and the Struve-H function, respectively, all of order  $\nu = 0$ . For distances  $r_0 \gg \lambda_p = 2\pi/Re[q_s^*]$ , the sum in brackets is very nearly equal to  $-\pi Y_0(q_s^* r)$ , which can be identified as the inhomogeneous part of the solution to the wave equation with open boundary conditions. The outgoing wave condition is therefore enforceable by an added homogeneous part  $\phi_h \propto i\pi J_0(q_s^* r)$ , in which case the term in square brackets becomes very nearly equal to  $i\pi H_0^1(q_s^* r)$ , with  $H_0^1(\dots)$  the Hankel function of the first kind of order  $\nu = 0$ , representing an outgoing cylindrical wave. Consequently, we forthwith augment the Fourier space propagator to enforce our prescribed boundary conditions:

$$\begin{aligned}
G(q) &= q_s^* \left( \frac{1}{q_s^* - q} + i\pi\delta(q - q_s^*) \right), \\
\text{so that } G_0(r) &\approx \frac{i}{2} q_s^{*2} H_0^1(q_s^* r).
\end{aligned} \tag{S11}$$

Here the Dirac delta function supplies the homogeneous component in Fourier space. Deviations not captured by this functional form at distances  $r \rightarrow 0$  associate with the “local” metallic response of the plasmonic medium, which supply screening of the incident divergent field as  $q_s^* \rightarrow 0$  in the limit where surface conductivity diverges to infinity. While this physical behavior is not captured by a mere wave solution, it remains inessential to our experimental results.

Meanwhile, the Fourier space representation for  $\hat{L}'$  operating on a function  $f(\mathbf{q})$  is:

$$[\hat{L}'f](\mathbf{q}) = \frac{1}{\epsilon q_s^*} \hat{\mathbf{q}} \cdot \int d^2q' 2\pi \Lambda(\mathbf{q} - \mathbf{q}') \mathbf{q}' f(\mathbf{q}') \tag{S12}$$

Here  $\hat{\mathbf{q}}$  denotes a unit wavevector, and real-space multiplication by  $\Lambda(\mathbf{r} - \mathbf{r}_0)$  within  $\hat{L}'$  is transformed by the convolution theorem into an integral kernel  $2\pi \Lambda(\mathbf{q} - \mathbf{q}')$ . Next, we apply the Fourier representation of the defect profile  $\Lambda(q) = e^{-i\mathbf{q}\cdot\mathbf{r}_0}/2\pi$  representing the Dirac delta function centered at  $\mathbf{r}_0$ , obtaining:

$$\begin{aligned}
[\hat{L}'f](\mathbf{q}) &= \frac{A_s}{\epsilon q_s^*} \hat{\mathbf{q}} \cdot \int d^2q' e^{-i(\mathbf{q}-\mathbf{q}')\cdot\mathbf{r}_0} \mathbf{q}' f(q') \\
&= \frac{A_s}{\epsilon q_s^*} e^{-i\mathbf{q}\cdot\mathbf{r}_0} \int_0^\infty dq' q'^2 f(q') \int_0^{2\pi} d\theta' \cos(\theta' - \theta) e^{iq'r_0 \cos\theta'} \\
&= \frac{2\pi i A_s}{\epsilon q_s^*} \cos\theta e^{-iqr_0 \cos\theta} \int_0^\infty dq' q'^2 J_1(q'r_0) f(q').
\end{aligned} \tag{S13}$$

Here  $J_1$  denotes the Bessel function of the first kind of order  $\nu = 1$ , and  $\theta'$  and  $\theta$  denote the angles subtended between the position vector  $\mathbf{r}_0$  and the incoming and outgoing wavevectors  $\mathbf{q}'$  and  $\mathbf{q}$ , respectively. Here we have also assumed  $f(\mathbf{q})$  to be an isotropic function. Since the defect-scattered field is given by  $\Delta\phi(\mathbf{r}) = \epsilon\hat{G}_0\hat{L}'\hat{G}_0\phi_{\text{probe}}(\mathbf{r})$ , then  $f = \hat{G}_0\phi_{\text{probe}}$ , and our point source at the origin is compatible with this assumption. The latter integral in Eq. (S13) can now be evaluated:

$$\begin{aligned}
f(q) &= [\hat{G}_0\phi_{\text{probe}}](q) = q_s^* \left( \frac{1}{q_s^* - q} + i\pi\delta(q - q_s^*) \right) \frac{A_p}{2\pi}, \quad \text{so that} \\
\int_0^\infty dq' q'^2 J_1(q'r_0) f(q') &= \frac{A_p q_s^*}{2\pi} \left[ i\pi q_s^{*2} J_1(q_s^* r_0) + \int_0^\infty dq' \frac{q'^2}{q_s^* - q'} J_1(q'r_0) \right] \\
&= \frac{A_p q_s^*}{2\pi} \left[ i\pi J_1(q_s^* r_0) - \frac{\partial}{\partial r_0} \int_0^\infty dq' \frac{q'}{q_s^* - q'} J_0(q'r_0) \right] \\
&= \frac{A_p q_s^{*2}}{2\pi} \left\{ i\pi q_s^* J_1(q_s^* r_0) - \frac{\partial}{\partial r_0} \left[ \frac{1}{q_s^* r} - \frac{\pi}{2} (Y_0(q_s^* r) + \mathbf{H}_0(q_s^* r)) \right] \right\}. \tag{S14}
\end{aligned}$$

Noting again that the sum in square brackets is very approximately equal to  $-\pi\partial_{r_0}Y_0(q_s^*r) = +\pi q_s^*Y_1(q_s^*r)$ , the sum in curled brackets is also very nearly equal to  $i\pi q_s^*H_1^1(q_s^*r_0)$ , a Hankel function of the first kind of order  $\nu = 1$ . Inserting this wave function back into Eq. (S13), we have:

$$\begin{aligned}
[\hat{L}'\hat{G}_0\phi_{\text{probe}}](\mathbf{q}) &= \left( \frac{2\pi i A_s}{\epsilon q_s^*} \cos\theta e^{-iqr_0 \cos\theta} \right) \times \frac{A_p q_s^{*2}}{2\pi} \times i\pi q_s^* H_1^1(q_s^* r_0) \\
&= -\frac{i\pi}{\epsilon} A_s A_p q_s^{*2} H_1^1(q_s^* r_0) \cos\theta e^{-iqr_0 \cos\theta} \tag{S15}
\end{aligned}$$

The field scattered by the defect can now be evaluated at the origin  $\mathbf{r} = \mathbf{0}$ , coinciding with the location of the probe field, as:

$$\begin{aligned}
\Delta\phi(\mathbf{r} = \mathbf{0}) &= \epsilon \int \frac{d^2q}{2\pi} [\hat{G}_0\hat{L}'\hat{G}_0\phi_{\text{probe}}](\mathbf{q}) \\
&= -i\pi A_s A_p q_s^{*3} H_1^1(q_s^* r_0) \int_0^\infty dq q \left( \frac{1}{q_s^* - q} + i\pi\delta(q - q_s^*) \right) \int_0^{2\pi} \frac{d\theta}{2\pi} \cos\theta e^{-iqr_0 \cos\theta} \\
&= +i\pi A_s A_p q_s^{*3} H_1^1(q_s^* r_0) \left[ i\pi q_s^* J_1(q_s^* r_0) + \int_0^\infty dq \frac{q}{q_s^* - q} J_1(qr_0) \right] \\
&\approx i\pi A_s A_p q_s^{*3} H_1^1(q_s^* r_0) \times -\frac{\partial}{\partial r_0} i\pi H_0^1(q_s^* r) \\
&\approx -(A_s q_s^{*2})(A_p q_s^{*2}) (\pi H_1^1(q_s^* r_0))^2. \tag{S17}
\end{aligned}$$

Here we have identified the term in square brackets as proportional to the  $r_0$ -derivative of our augmented propagator  $G_0(r = r_0)$ , for which we readily supply the outgoing wave approximation (Eq. (S11)).

We note that the two leading dimensionless terms in parentheses in Eq. (S17) scale as the perturbation area in comparison to the plasmon wavelength  $\lambda_p = 2\pi/q_s^*$  squared. In the context where graphene nanobubbles scatter plasmon polariton fields with momentum  $q_s^*$ , the defect area is described by  $A_s = -\pi R_{\text{bubble}}^2$  (negation implying a deficit of conductivity) and the perturbation treatment applied here is self-consistent so long as  $R_{\text{bubble}} \ll \lambda_p$ . Since excitation from the near-field probe may be described by  $A_p \sim a^2$  with  $a$  the probe tip radius, the condition  $a < \lambda_p$  implies the perturbation treatment here should be a particularly robust description of our experiments. Our nano-imaging experiments approximately detect the vertically polarized field scattered on the graphene surface. This field is proportional to instantaneous surface charge on the graphene, which is in turn proportional to  $\Delta\phi(\mathbf{r})$ . Taking  $r_0$  as the probe-nanobubble separation distance, we can therefore directly apply the complex-valued functional form  $H_1^1(q_s^* r_0)^2$  to fit the line-profiles presented in Figure 3C of the main text. This form is characterized by alternating fringes with an apparent spatial period of  $\lambda_p/2$ , owing to round-trip traversal of polariton fields over a cumulative distance  $2r_0$  between the probe and the nanobubble and back. This formalism therefore supplies a quantitative means to extract plasmon polariton momentum and wavelength directly from our nano-infrared images.

## References

- [1] Girit, Ç. Ö. & Zettl, A. Soldering to a Single Atomic Layer. *Applied Physics Letters* **91**, 193512, (2007).
- [2] May, A. F., Yan, J. & McGuire, M. A. A Practical Guide for Crystal Growth of Van Der Waals Layered Materials. *Journal of Applied Physics* **128**, 051101, (2020).
- [3] Kresse, G. & Furthmüller, J. Efficient Iterative Schemes for Ab Initio Total-Energy Calculations Using a Plane-Wave Basis Set. *Physical Review B* **54**, 11169-11186, (1996).
- [4] Perdew, J. P., Burke, K. & Ernzerhof, M. Generalized Gradient Approximation Made Simple. *Physical Review Letters* **77**, 3865-3868, (1996).
- [5] Klimeš, J., Bowler, D. R. & Michaelides, A. Van Der Waals Density Functionals Applied to Solids. *Physical Review B* **83**, 195131, (2011).
- [6] Andrade, X., Strubbe, D., De Giovannini, U., Larsen, A. H., Oliveira, M. J. T., Alberdi-Rodriguez, J., Varas, A., Theophilou, I., Helbig, N., Verstraete, M. J., Stella, L., Nogueira, F., Aspuru-Guzik, A., Castro, A., Marques, M. A. L. & Rubio, A. Real-Space Grids and the Octopus Code as Tools for the Development of New Simulation Approaches for Electronic Systems. *Physical Chemistry Chemical Physics* **17**, 31371-31396, (2015).
- [7] Tancogne-Dejean, N., Oliveira, M. J. T., Andrade, X., Appel, H., Borca, C. H., Le Breton, G., Buchholz, F., Castro, A., Corni, S., Correa, A. A., De Giovannini, U., Delgado, A., Eich, F. G., Flick, J., Gil, G., Gomez, A., Helbig, N., Hübener, H., Jestädt, R., Jornet-Somoza, J., Larsen, A. H., Lebedeva, I. V., Lüders, M., Marques, M. A. L., Ohlmann, S. T., Pipolo, S., Rampp, M., Rozzi, C. A., Strubbe, D. A., Sato, S. A., Schäfer, C., Theophilou, I., Welden, A. & Rubio, A. Octopus, a Computational Framework for Exploring Light-Driven Phenomena and Quantum Dynamics in Extended and Finite Systems. *The Journal of Chemical Physics* **152**, 124119, (2020).
- [8] Tancogne-Dejean, N., Oliveira, M. J. T. & Rubio, A. Self-Consistent *Dft+U* Method for Real-Space Time-Dependent Density Functional Theory Calculations. *Physical Review B* **96**, 245133, (2017).
- [9] Agapito, L. A., Curtarolo, S. & Buongiorno Nardelli, M. Reformulation of *Dft+U* as a Pseudohybrid Hubbard Density Functional for Accelerated Materials Discovery. *Physical Review X* **5**, 011006, (2015).
- [10] Rejaei, B. & Khavasi, A. Scattering of Surface Plasmons on Graphene by a Discontinuity in Surface Conductivity. *Journal of Optics* **17**, 075002, (2015).
- [11] Jing, R., Shao, Y., Fei, Z., Lo, C. F. B., Vitalone, R. A., Ruta, F. L., Staunton, J., Zheng, W. J. C., McLeod, A. S., Sun, Z., Jiang, B.-y., Chen, X., Fogler, M. M., Millis, A. J., Liu, M., Cobden, D. H., Xu, X. & Basov, D. N. Terahertz Response of Monolayer and Few-Layer Wte2 at the Nanoscale. *Nature Communications* **12**, 5594, (2021).
- [12] Nikitin, A., Alonso-González, P., Vélez, S., Mastel, S., Centeno, A., Pesquera, A., Zurutuza, A., Casanova, F., Hueso, L. & Koppens, F. Real-Space Mapping of Tailored Sheet and Edge Plasmons in Graphene Nanoresonators. *Nature Photonics* **10**, 239-243, (2016).
- [13] Prudnikov, A. P., Brychkov, I. U. A. & Marichev, O. I. *Integrals and Series: Special Functions*. Vol. 2 (CRC press, 1986).